JGR Space Physics

RESEARCH ARTICLE
10.1029/2018JA026290

The Role of Current Sheet Scattering in the Proton Isotropic Boundary Formation During Geomagnetic Storms

John D. Haiducek[1], **Natalia Y. Ganushkina**[2,3], **Stepan Dubyagin**[3], **and Daniel T. Welling**[2,4]

[1]U.S. Naval Research Laboratory, Washington, DC, USA, [2]Climate and Space Sciences, University of Michigan, Ann Arbor, MI, USA, [3]Finnish Meteorological Institute, Helsinki, Finland, [4]University of Texas at Arlington, Arlington, TX, USA

Key Points:
- We corrected estimates of the adiabaticity parameter K using in situ data, obtaining consistent results between empirical and MHD models
- A significant fraction of the K estimates was below the threshold for current sheet scattering
- Corrected K estimates are independent of *Sym-H** and MLT, even for high values of K

Supporting Information:
- Supporting Information S1
- Data Set S1
- Data Set S2
- Data Set S3

Correspondence to:
J. Haiducek,
jhaiduce@umich.edu

Citation:
Haiducek, J. D., Ganushkina, N. Y., Dubyagin, S., & Welling, D. T. (2019). The role of current sheet scattering in the proton isotropic boundary formation during geomagnetic storms. *Journal of Geophysical Research: Space Physics*, *124*, 3468–3486. https://doi.org/10.1029/2018JA026290

Received 12 NOV 2018
Accepted 24 APR 2019
Accepted article online 1 MAY 2019
Published online 31 MAY 2019

Abstract There is considerable evidence that current sheet scattering (CSS) plays an important role in isotropic boundary (IB) formation during quiet time. However, IB formation can also result from scattering by electromagnetic ion cyclotron waves, which are much more prevalent during storm time. The effectiveness of CSS can be estimated by the parameter $K = \frac{R_c}{r_g}$, the ratio of the field line radius of curvature to the particle gyroradius. Using magnetohydrodynamic and empirical models, we estimated the parameter K associated with storm time IB observations on the nightside. We used magnetic field observations from spacecraft in the magnetotail to estimate and correct for errors in the K values computed by the models. We find that the magnetohydrodynamic and empirical models produce fairly similar results without correction and that correction increases this similarity. Accounting for uncertainty in both the latitude of the IB and the threshold value of K required for CSS, we found that 29–54% of the IB observations satisfied the criteria for CSS. We found no correlation between the corrected K and magnetic local time, which further supports the hypothesis that CSS played a significant role in forming the observed IBs.

1. Introduction

During geomagnetic storms, the shape and structure of the magnetotail can change rapidly and dramatically. This includes changes in the orientation of the current sheet, as well as rapid stretchings and dipolarizations. Although storms are driven by the solar wind, the ionosphere plays an important role in regulating the geomagnetic response to these solar wind inputs (e.g., Brambles et al., 2011, 2013; Daglis, 1997; Glocer et al., 2009; Welling & Liemohn, 2016). As such, characterizing the connections and interaction between the ionosphere and the magnetotail during storms is necessary in order to fully understand the behavior of the magnetosphere during storm conditions.

Most interaction between the magnetosphere and the ionosphere occurs through the flow of particles and currents along magnetic field lines. Characterizing the structure of these field lines can help us to determine the origins and destinations of plasma flows between the magnetosphere and ionosphere and thus to better understand how the two regions interact with each other. Unfortunately, our ability to determine field line structure is limited by the very sparse distribution of satellite observations throughout much of the magnetosphere. As a result, models of field line structure are often poorly constrained, particularly during storm conditions when rapid changes in field line shape pose an added challenge in determining the global system state at any given time.

To supplement the sparse magnetospheric observations, ionospheric observations can be used to help better determine the state of the magnetotail. Ionospheric observations have the advantage of being at a low altitude where relatively large numbers of satellites with fairly short orbital periods provide much better data coverage than is available in most of the magnetosphere. For instance, at present three National Oceanic and Atmospheric Administration (NOAA) Polar Orbiting Environmental Satellites (POES) satellites are in operation at altitudes of 800–900 km and with orbital periods around 100 min (https://www.ospo.noaa.gov/Operations/POES/status.html). Similarly, two METOP satellites are in orbit at an 817-km altitude (https://www.eumetsat.int/website/home/Satellites/CurrentSatellites/Metop/index.html),

and several Defense Meteorological Satellite Program spacecraft orbit at a nominal 850-km orbit (http://www.au.af.mil/au/awc/space/factsheets/dmsp.htm).

In order to leverage ionospheric observations to help determine magnetotail structure, we must identify a feature in the ionosphere that maps to a known location in the magnetosphere (or at least, to a location with known characteristics). This is the case for the isotropic boundary (IB), which is a feature in the auroral zone of the ionosphere characterized by a substantial change in the flux of downwelling particles. Poleward of the IB, comparable fluxes are observed in directions parallel to and perpendicular to the local magnetic field, while equatorward of the IB the flux in directions perpendicular to the local magnetic field is much greater than the flux in the parallel direction. This tendency has been observed by a number of satellites, including Injun 1 and 3, ESRO IA and IB, NOAA, and Defense Meteorological Satellite Program (Newell et al., 1998; Imhof et al., 1977; Sergeev et al., 1983; Søraas, 1972). The proton IB is observed at all activity levels and in all magnetic local time (MLT) sectors (Sergeev et al., 1993).

The change in loss cone filling observed as a spacecraft transits the IB indicates that the IB maps to a transitional region in the magnetosphere, which is characterized by a substantial change in the rate of pitch angle scattering. Two mechanisms for this have been proposed. Current sheet scattering (CSS) refers to a process in which particles undergo chaotic motion upon crossing the current sheet, resulting in changes to the particles' pitch angles (Büchner & Zelenyi, 1987; Sergeev et al., 1993; West et al., 1978). This occurs when the radius of curvature, R_c, and the effective particle gyroradius, r_g, become comparable to each other, resulting in a violation of the first adiabatic invariant (Alfvén & Fälthammar, 1963; Büchner & Zelenyi, 1987; Delcourt et al., 1996; Tsyganenko, 1982). The second mechanism that has been proposed for IB formation is the scattering of particles by electromagnetic ion cyclotron (EMIC) waves, in which plasma waves having oscillations near the particle gyrofrequency result in a violation of the first adiabatic invariant (Kennel & Petschek, 1966; Liang et al., 2014; Sergeev, Chernyaeva, Angelopoulos, et al., 2015; Sergeev, Chernyaeva, Apatenkov, et al. 2015).

Of the two mechanisms, the CSS process operates at all times and in all MLT sectors. A number of papers have identified CSS as the main (though not necessarily exclusive) mechanism for IB formation during quiet time (Ganushkina et al., 2005; Haiducek et al., 2019; Sergeev & Tsyganenko, 1982; Sergeev et al., 1993). However, at times EMIC scattering may cause the IB to be observed at a lower latitude than would occur if CSS were the operative mechanism. This occurs primarily during storms and substorms (Dubyagin et al., 2018; Gvozdevsky et al., 1997; Sergeev et al., 2010; Søraas et al., 1980; Yahnin & Yahnina, 2007), though there is evidence that it occurs during quiet times as well (e.g., Popova et al., 2018; Sergeev, Chernyaeva, Angelopoulos, et al., 2015).

Distinguishing whether CSS or EMIC is the responsible mechanism for a particular IB observation is necessary for the application of IB observations to estimating magnetotail field geometry. When CSS is the responsible mechanism, the IB latitude can be used to estimate the amount of field line stretching in the magnetotail (Meurant et al., 2007; Sergeev et al., 1993; Sergeev & Gvozdevsky, 1995). This approach is likely to work well during quiet periods, but during storms it is expected that EMIC scattering will play a more significant role than it does in quiet time, because EMIC waves are more prevalent during storms. For instance, Erlandson and Ukhorskiy (2001) found that the EMIC wave occurrence rate increases by a factor of 5 during storm conditions over 10 years of observations, and Halford et al. (2010) also found an increased EMIC occurrence rate during storm conditions. Determining whether EMIC or CSS is responsible for IB formation at a given time and longitude requires estimating the value $K = \frac{R_c}{r_g}$ associated with a given IB observation. K parameterizes the effectiveness of the CSS process. Sergeev et al. (1983) proposed $K \leq 8$ as a threshold condition for CSS scattering, while Delcourt et al. (1996, 2000, 2006) showed that CSS operates when $K \lesssim 1$–10, and Sergeev, Chernyaeva, Angelopoulos, et al. (2015) suggested that CSS could be responsible for IB formation with K as high as 12. In the present work, recognizing that no single value of K can be regarded as the definitive threshold, we adopt the range $K = 8$–13 as a nominal uncertainty range for the CSS scattering threshold, where the commonly used $K \leq 8$ threshold serves as the lower end of the uncertainty range and the $K \leq 13$ value as the upper end of the uncertainty range, following the recent study by Dubyagin et al. (2018).

Computing K values associated with an IB observation requires tracing a magnetic field line from the location of the observation to the point where it crosses the current sheet. Both steps require a magnetic field model that can provide field vectors at arbitrary points within the magnetosphere. Most previous studies

to do this have employed empirical models such as the Tsyganenko models (e.g., Dubyagin et al., 2018; Ganushkina et al., 2005; Sergeev, Chernyaeva, Angelopoulos, et al., 2015; Sergeev et al., 1993), but two have done so using magnetohydrodynamic (MHD) models (e.g., Haiducek et al., 2019; Ilie et al., 2015). Ilie et al. (2015) obtained K values for IB observations during a quiet period and obtained unrealistically high K values for conditions in which CSS was expected to be the dominant mechanism. Haiducek et al. (2019) simulated the same quiet period using different model settings. Haiducek et al. (2019) obtained lower K values than those of Ilie et al. (2015) and demonstrated that these values could be corrected using in situ magnetic field observations, concluding that the quiet time IB observations were likely the result of CSS and not EMIC.

The work of Haiducek et al. (2019) demonstrated the use of MHD to estimate K during quiet conditions and obtained results that were consistent with those derived from empirical models for the same time period. However, the circumstances in which MHD is likely to be most advantageous for studying the IB are during storm conditions. Through simulations of storms, the physics incorporated into an MHD model can be used to shed light on the causes of storm time dynamics. Several previous papers have presented K estimates during storm conditions, but all have used empirical models that were constructed from fits to historical satellite observations (e.g., Dubyagin et al., 2018; Ganushkina et al., 2005; Sergeev et al., 1993). Since MHD models simulate the physics of the magnetosphere rather than presenting a fit to historical observations, it has the potential to reproduce features and dynamics of storm events that may be missed by empirical models, as well as provide additional information that can shed light on the causes of any dynamics that are reproduced by the model. The use of MHD to explore IB properties during disturbed conditions (specifically, during a substorm) was previously demonstrated by Gilson et al. (2012), but no comparison of K estimates with IB observations was performed. To date, no published work has used MHD to explore IB properties during a geomagnetic storm.

The goal of the present work is to estimate what fraction of IB observations might be the result of CSS during storm conditions and to test whether MHD and empirical models produce consistent values of K during storm conditions. We estimate K using multiple MHD simulations and multiple empirical models, in order to obtain a better representation of the range of variability for K than would be possible using any single model alone. Next we compare our K values with the $K = 8$ and $K = 13$ threshold conditions to estimate what fraction of the IB observations may have been the result of CSS (as opposed to EMIC wave scattering). We estimate errors in the model output by comparing with in situ magnetic field observations and apply procedures from Dubyagin et al. (2018) and Haiducek et al. (2019) to correct for these errors. The present work is the first to use MHD to explore IB properties during a geomagnetic storm and the first to estimate K using MHD during disturbed conditions.

The paper is organized as follows. Section 2 provides a description of the time period chosen and the observational data used. Section 3 describes the procedures used to estimate K and the details of the MHD simulations. Section 4 presents a validation of the MHD magnetic fields against in situ observations. Sections 5 and 6 present results from the MHD and empirical models, respectively. Section 7 outlines the procedure for correcting the K values and presents the overall results for K and the corrections, and the paper concludes with section 8.

2. Event and Observations

We chose the time period of 2100 UT on 4 April 2010 to 1400 UT on 6 April 2010 for our analysis. The major feature of this time period is a moderate storm with a minimum *Sym-H* of −90 nT and a maximum *Kp* of 7.7. This storm was the result of a coronal mass ejection observed at 0954 UT 3 April. The northern flank of the coronal mass ejection reached the Sun-Earth L1 Lagrange point around 0755 UT on 4 April and was followed by the passage of a magnetic cloud from around 1200 UT on 5 April to 1320 UT on 6 April (Liu et al., 2011; Möstl et al., 2010). Solar wind parameters from this time period are shown in Figures 1a–1d. The beginning of the storm is marked with a vertical line. Observational data shown in Figure 1 come from the 1-min OMNI data set provided by the National Aeronautics and Space Administration Goddard Space Flight Center. The beginning of the storm is marked by a sudden increase in solar wind speed between 0800 and 0900 UT on 5 April (see the u_x velocity component in Figure 1a), accompanied by sharp increases in solar wind density ρ (Figure 1b) and temperature (Figure 1c). The B_z component of the interplanetary magnetic field (Figure 1d) abruptly became more negative at the same time and oscillated rapidly for the next few hours.

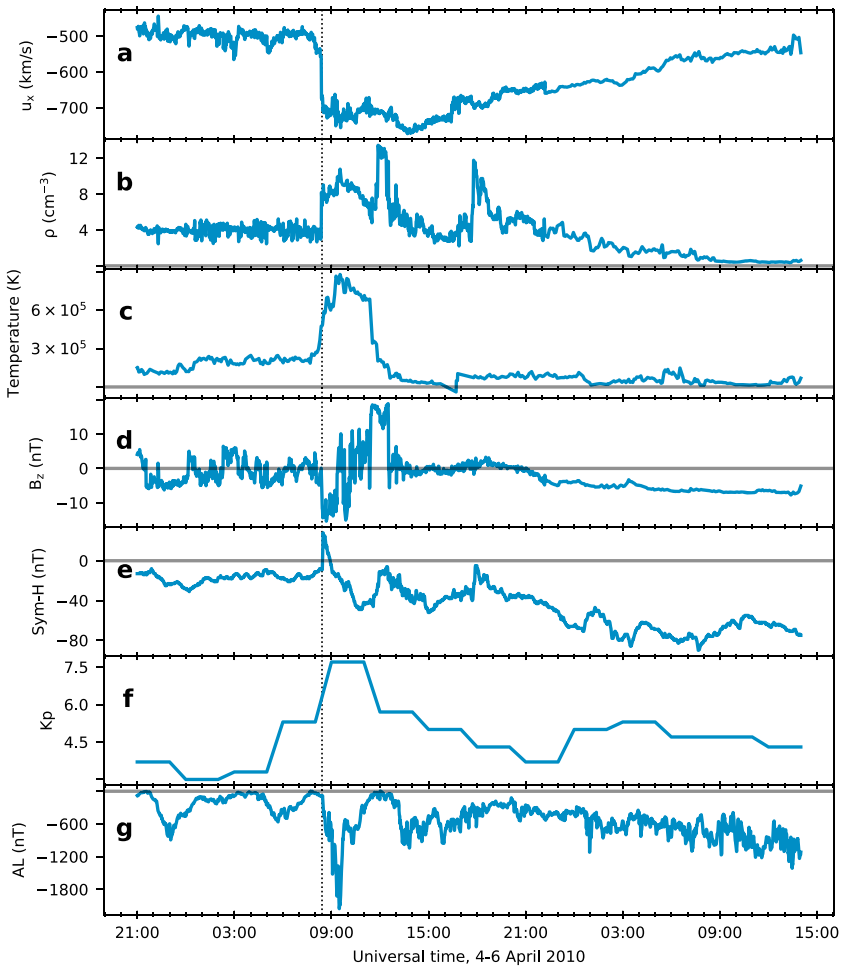

Figure 1. Solar wind driving parameters used in the study, along with geomagnetic indices parameterizing the magnetospheric response. (a) u_x component of bulk velocity, in geocentric solar magnetospheric coordinates, (b) proton density ρ, (c) temperature, (d) interplanetary magnetic field B_z, (e) *Sym-H*, and (f) *Kp*, (g) *AL*. The beginning of the storm is marked with a vertical line.

To quantify the magnetospheric response to the storm, we use the *Sym-H*, *Kp*, and *AL* indices. The latitude of the IB has been found to be sensitive to all three of *Sym-H* (e.g., Asikainen et al., 2010; Dubyagin et al., 2013, 2018; Ganushkina et al., 2005; Hauge & Söraas, 1975; Lvova et al., 2005; Søraas, 1972; Søraas et al., 2002), *Kp* (e.g., Søraas, 1972; Sergeev et al., 1993; Yue et al., 2014), and *AL* (e.g., Dubyagin et al., 2013; Lvova et al., 2005; Søraas, 1972).

The *Sym-H*, *Kp*, and *AL* indices during 4–6 April 2010 are shown in Figures 1e–1g. From the *Sym-H* index (Figure 1e), a storm sudden commencement can be seen just after 0800 UT on 5 April, followed by a sharp decrease in *Sym-H*. The minimum *Sym-H* of −90 nT does not occur until almost 24 hr later. The maximum *Kp* of 7.7 occurred around 0900 UT on 5 April (Figure 1f), and *Kp* remained at or above 3 throughout the event. The *AL* index (Figure 1g) dropped rapidly after the storm commencement, reaching a minimum of −2,152 nT but quickly recovering.

Observations of isotropic boundaries were obtained using the Medium Energy Proton and Electron Detector (MEPED) instruments (Evans & Greer, 2000) onboard five NOAA/POES and one METOP spacecraft. This instrument consists of two telescopes that detect proton fluxes in four energy bands between 30 and 6,900 keV. The telescopes are referred to as the 0° and 90° telescopes, after their approximate directions relative to the spacecraft's zenith. The 0° telescope points away from the Earth, while the 90° telescope is roughly perpendicular to the 0° telescope and points along the spacecraft's velocity vector. When the spacecraft

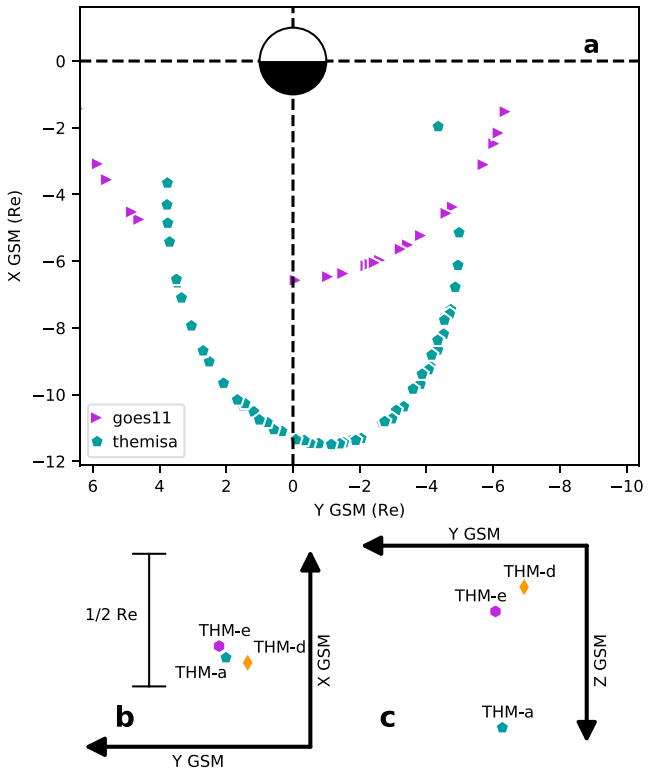

Figure 2. (a) Locations of THEMIS A and GOES 11 at the times of all the isotropic boundary observations. (b and c) Relative positions of THEMIS A, THEMIS D, and THEMIS E at 0700 UT on 5 April.

is at relatively high latitudes, this configuration results in the 0° telescope mainly detecting precipitating particles, while the 90° telescope mainly detects locally trapped particles.

IB locations were identified from the MEPED P1 energy channel. The nominal energy range of this channel is 30–80 keV, but in reality the lower-energy limit is somewhat higher than 30 keV and varies among the satellites due to degradation of the detectors over time. We used the low-energy limits given by Asikainen et al. (2012), and these are reproduced in Table S1 in the supporting information. In addition to variance between the spacecraft, the 90° telescope degrades more rapidly than the 0°. We recalibrate the 90° flux to correspond to the 0° cutoff energy using the procedure given in the appendix of Dubyagin et al. (2018). Using these corrected fluxes, we found IB crossings with the procedure described in Dubyagin et al. (2018). It should be noted that there can be significant uncertainty associated with the determination of IB locations from MEPED data during storm periods. To address this, the Dubyagin et al. (2018) procedure defines a high-latitude (HL) and low-latitude (LL) limit of the IB based on the MEPED data, which we use to estimate the uncertainty range for the IB latitude.

Rather than using all available IB observations, we limit our analysis to those for which in situ magnetic field observations were available in the magnetotail from one or more spacecraft that were conjugate with the location of the IB observation in the ionosphere. To consider a spacecraft as conjugate with the IB observation, we require it be within one hour MLT of the location of the IB observation. In addition, we require the conjugate spacecraft to be located near the equatorial plane between 4 and 12 R_E from the Earth. Only IB observations from the nightside were used. The spacecraft meeting these criteria were Time History of Events and Macroscale Interactions during Substorms (THEMIS A, THEMIS D, and THEMIS E; Auster et al., 2008; McFadden, Carlson, Larson, Bonnell, et al., 2008; McFadden, Carlson, Larson, Ludlam at al., 2008), and Geostationary Operational Environmental Satellite (GOES 11 to GOES 15; Singer et al., 1996). Representative locations for these spacecraft are shown in Figure 2. In total, 127 HL IB observations and 127 LL IB observations were found on the nightside for which at least one of the GOES or THEMIS satellites was conjugate with the IB observation. Exact times and locations of each IB observation are provided in the supporting information.

Figure 2a shows examples of conjugate satellite positions in the *x*-*y* geocentric solar magnetospheric (GSM) plane, with THEMIS A locations marked with turquoise pentagons and GOES 11 locations with purple triangles. THEMIS D and THEMIS E, not shown, had orbits somewhat similar to that of THEMIS A, while GOES 12–15 were in geosynchronous orbits similar to that of GOES 11. Satellite locations were obtained using orbital data from the Satellite Situation Center Web (https://sscweb.gsfc.nasa.gov). The markers in Figure 2a show satellite positions for all the times at which the respective satellite was conjugate with an IB observation.

Figures 2b and 2c show the relative positions of THEMIS A, THEMIS D, and THEMIS E at 0700 UT on 5 April, when all three were near apogee. Figure 2b shows the *x*-*y* (GSM) plane, while Figure 2c shows the *y*-*z* plane. THEMIS E is depicted as a purple hexagon, and THEMIS D as an orange diamond. Note that the spacecraft are spaced relatively closely in *x* and *y*, but THEMIS A is separated significantly in the *z* direction from THEMIS D and THEMIS E. This configuration allows the estimation of gradients in the *z* direction by computing a difference between THEMIS A and THEMIS E. Configurations like this existed a significant part of the time interval under study, and we used such satellite configurations to estimate R_c and its influence on *K*.

3. Methodology

For each of the 227 IB crossings identified as described in the previous section, we trace a magnetic field line from the location of the IB observation and compute $K = \frac{R_c}{r_g}$ at the point along the field line that is farthest from the Earth. Both the field line tracing and the computation of K require a model to estimate the magnetic fields. For this purpose we use MHD simulations executed using the Space Weather Modeling Framework (SWMF; Tóth et al., 2005) and the T01 (Tsyganenko, 2002), TS05 (Tsyganenko & Sitnov, 2005), and TA16 (Tsyganenko & Andreeva, 2016) empirical magnetic field models. The setup for the SWMF simulations is described in detail later in this section, and the empirical models are described in section 6.

The point of maximum distance from the Earth was chosen as an estimate of where the field line crosses the current sheet. Although intuitively the point of minimum $|\mathbf{B}|$ would indicate the current sheet, we found that in some cases the field line is "pinched" around the current sheet, producing an additional pair of local minima in $|\mathbf{B}|$, which are sometimes lower than the minimum that occurs when the field line crosses the current sheet. As a result the maximum distance proved to be a more robust indicator of where the field line crossed the current sheet. In a few cases the field line traced from the IB location was found to be open (extending outside the MHD domain), and such cases were excluded from further analysis.

At the point of maximum distance from the Earth along the field line, we compute R_c, the field line radius of curvature, given by

$$R_c = \frac{1}{|(\mathbf{b} \cdot \nabla)\mathbf{b}|}, \tag{1}$$

where $\mathbf{b}$ is the unit vector in the direction of the local magnetic field. The gradient $\nabla\mathbf{b}$ is computed using a two-point centered difference scheme on the MHD grid. The effective gyroradius r_g is computed for protons whose energy is equal to the low energy limit of the respective detector, as given in Table S1 in the supporting information. We then use these estimates of R_c and r_g to compute K. We rejected any K estimates below 0.01.

Our SWMF simulations use the Block Adaptive Tree Solar-Wind, Roe-type Upwind Scheme MHD code (DeZeeuw et al., 2000; Powell et al., 1999). This is coupled with the Rice Convection Model (Sazykin, 2000; Toffoletto et al., 2003; Wolf et al., 1982) and the Ridley Ionosphere Model (Ridley & Liemohn, 2002; Ridley et al., 2004). The inputs to the model are solar wind parameters (velocity, density, temperature, and magnetic field) and $F10.7$ solar radio flux, as shown in Figure 1. Solar wind parameters were obtained from the 1-min OMNI data set. $F10.7$ flux was obtained from the noontime flux observed at Penticton, British Columbia, and published online (ftp://ftp.geolab.nrcan.gc.ca/data/solar_flux/daily_flux_values/fluxtable.txt; Tapping, 2013).

We ran three SWMF simulations, with the same inputs but with different grid resolutions and differences in numerical schemes and coupling parameters. By comparing the results obtained with the three simulations, we are able to assess qualitatively how sensitive the model-derived K values are to the model settings. The three simulations are the same as those in Haiducek et al. (2019), and details on the settings can be found there and in Haiducek et al. (2017), which shares some of the settings in common. We describe them briefly here:

1. *SWMFa*: Same settings as Ilie et al. (2015), but with modifications to improve stability (details in Haiducek et al., 2019). Four million cell grid, with a 0.25 R_E cell size in the expected region of IB formation.
2. *SWMFb*: A 2 million cell grid, with a finer resolution the midtail (48–120 R_E) compared with SWMFa, but courser resolution farther downtail (beyond 120 R_E). A 0.25 R_E cell size in the expected region of IB formation. Settings described in detail in Haiducek et al. (2017) where this model configuration is referred to as the "Hi-res" configuration.
3. *SWMFc*: A 1 million cell grid with settings based on those used operationally by the NOAA Space Weather Prediction Center. A 0.5 R_E cell size in the expected region of IB formation. Settings are described in detail in Haiducek et al. (2017), where this model configuration is referred to as the "SWPC" configuration.

During execution of the simulations, magnetic field lines were traced from the locations of each IB observation once every minute of simulation time. Within the MHD domain, the field lines were traced using a third-order Runge-Kutta scheme with a second-order error estimation and adaptive step size. Since the inner boundary of the MHD domain was set to 2.5 R_E, well above the altitude of the IB observations, the IB locations were mapped to 2.5 R_E prior to tracing through the MHD domain. This was done by transforming

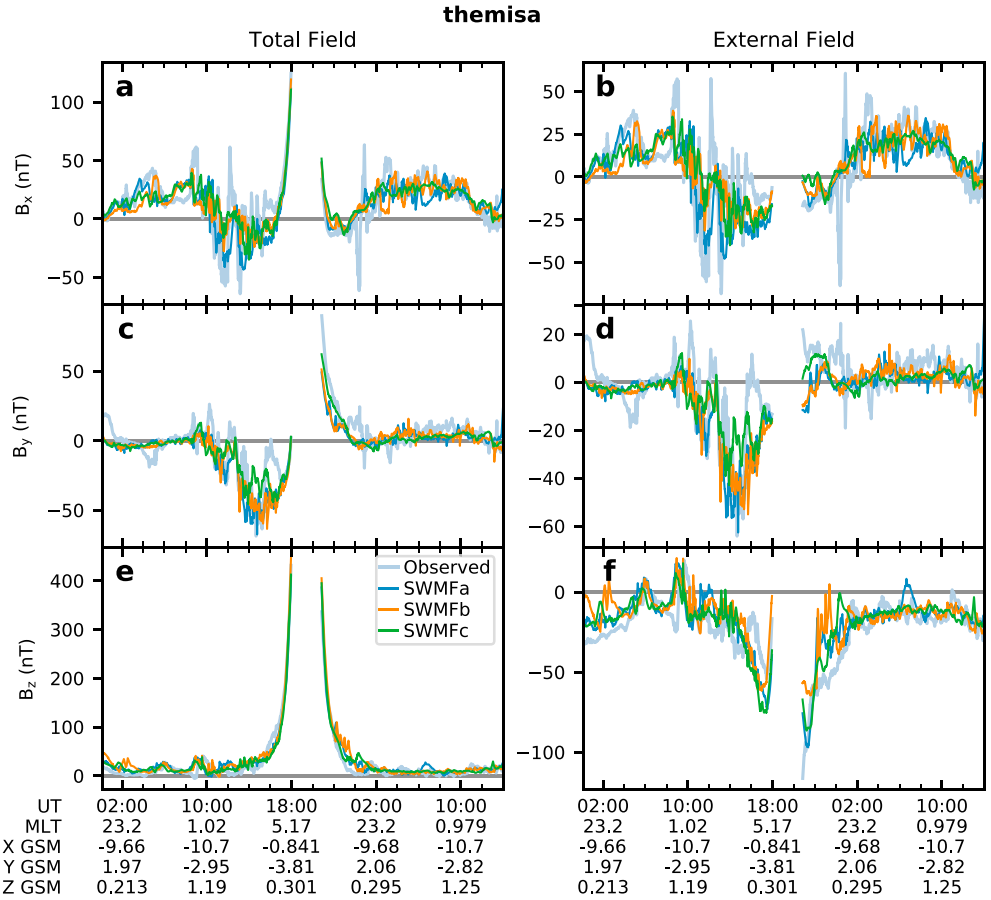

Figure 3. Magnetic field components of the total field in GSM coordinates at the THEMIS A satellite, observed and simulated, from 0009 UT on 5 April to 1400 UT on 6 April 2010. MLT = magnetic local time; GSM = geocentric solar magnetospheric; SWMF = Space Weather Modeling Framework.

the IB locations into altitude adjusted corrected geomagnetic coordinates (AACGM; Baker & Wing, 1989) with the reference height set to 0 km and then mapping to 2.5 R_E using a dipole field. The use of AACGM coordinates minimizes the influence of non dipole harmonics on the mapping.

4. Comparison of MHD Magnetic Fields With In Situ Observations

Before analyzing the IB observations using MHD, we made a comparison of the MHD magnetic fields with in situ observations. This provides a means to verify that the simulation accurately reproduces the magnetic field in the magnetotail. An example of this comparison is shown in Figure 3, which contains plots of simulated and observed magnetic fields along the orbit of the THEMIS A satellite. (Similar plots for THEMIS D and THEMIS E and GOES 11 to GOES 15 are included in the supporting information.) Figures 3a, 3c, and 3e show the x, y, and z (GSM) components of the total magnetic field, while Figures 3b, 3d, and 3f show the same for the external field. In all of these plots, the observed field is depicted as a light blue curve, and the SWMFa, SWMFb, and SWMFc simulations are shown as thinner curves colored in medium blue, orange, and green, respectively. THEMIS data were downloaded and calibrated using the THEMIS Data Analysis Software (http://themis.ssl.berkeley.edu/software.shtml). Magnetic field data are shown only for times when the satellite was at least 4 R_E away from the Earth, since closer locations do not satisfy our selection criteria for analysis. The time period shown is 0009 UT on 4 April to 1400 UT on 6 April 2010, an interval that includes the times of all the IB observations used in this study.

The external magnetic field shown in Figures 3b, 3d, and 3f was obtained by removing dipole component of the Earth's intrinsic field, evaluated using Geopack (http://geo.phys.spbu.ru/~tsyganenko/modeling.html). We remove only the dipole component because that is how the intrinsic field is represented within SWMF. As

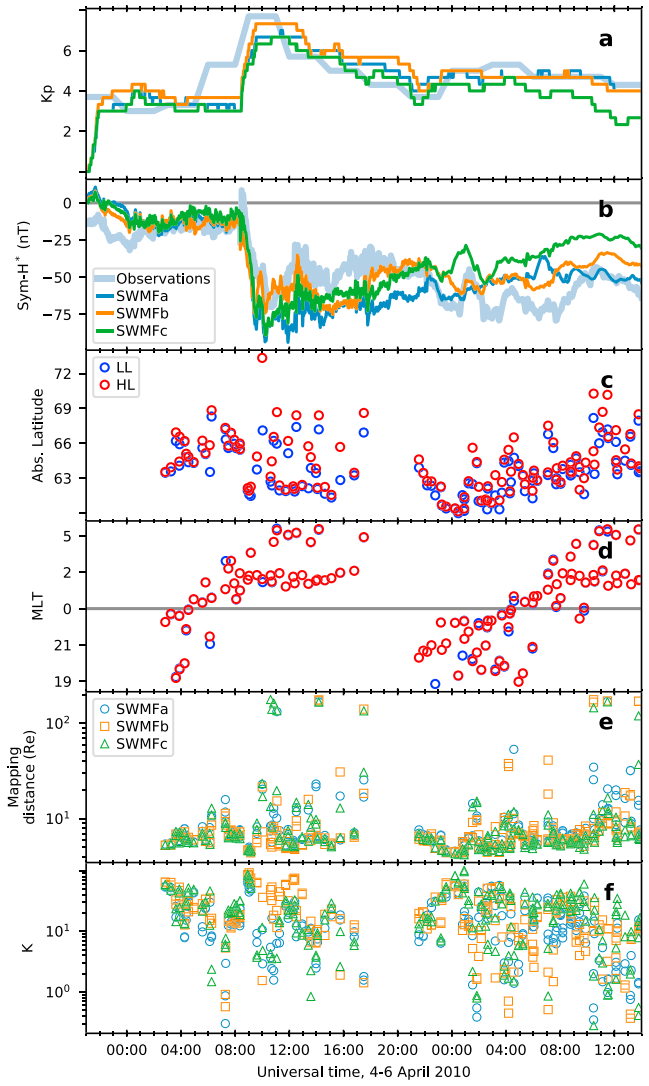

Figure 4. Isotropic boundary (IB) parameters and geomagnetic indices as a function of time. (a) *Kp* index, observed and simulated, (b) *Sym-H** index, observed and simulated, (c) absolute value of magnetic latitude of the IB observations, (d) magnetic local time of the IB observations, (e) maximum downtail distance of the field lines mapped from the IB locations, for each of the three magnetohydrodynamic simulations, and (f) *K* computed from the magnetohydrodynamic solution at the farthest point of each field line.

mentioned in the previous section, the influence of nondipole harmonics on the K estimations is minimized by converting the IB locations to AACGM coordinates prior to tracing the fields in SWMF. Points where the spacecraft is closer than 4 R_E to the Earth have been excluded from the plot, since such points do not meet the criteria for selection of conjugate points with IB observations.

Multiple sign changes in B_x can be seen in Figure 3a, which are indicative of current sheet crossings. This occurs most noticeably between 0900 and 1600 UT on 5 April during the initial phases of the storm, and a few additional current sheet crossings occur between 2100 and 0200 UT on 5–6 April and around 1200 on 6 April.

From Figure 3, it can be seen that the SWMF simulations reproduce many of the major variations in the observed field. During the quiet period before the storm, the error generally remains within 25 nT in all three components (Figures 3b, 3d, and 3f).

At the storm sudden commencement around 0900 UT on 5 April, a sharp increase in observed B_z occurs, and is accompanied by an increase in B_x and oscillations in B_y. Similar behavior occurs in the simulations, but the timing is slightly different and the variation in B_x and B_y is weaker than observed. After the storm sudden commencement, all three simulations reproduce the general trend in the observations, in which B_x and B_y become more negative, and B_z increases sharply and then decreases. Like the observations, rapid fluctuations in B_x and B_y are apparent, though the magnitude of these fluctuations is weaker and the timing is not exactly the same as the observations. In some cases this results in particularly large magnetic field errors such as the spike in B_x around 1200 UT on 5 April, which was not reproduced by any of the simulations. The somewhat weaker magnitude of oscillations in the model output may indicate a thicker or weaker current sheet compared with reality. From about 1300 to 1800 UT on 5 April the simulations produce more negative B_x than observed, which suggests that the model current sheet is more northerly than actual during that time, or that the current in the model is stronger than actual. During the next orbit of the spacecraft (2100 UT on 5 April to 1400 UT on 6 April) the conditions are somewhat quieter, with the largest disturbance being a brief but substantial (≈60 nT) oscillation in B_x and B_y around 2400 UT and a weaker one around 0300 UT, neither of which is reproduced by the simulations. Some fairly large (≈50 nT) errors occur in SWMFb between 2200 and 2400. Aside from the aforementioned periods, the simulation fields during the second orbit remained generally within 20 nT of the observations.

5. MHD Results

Figure 4 shows the behavior of the *Kp* and *Sym-H* indices and the IB mapping parameters over the course of the storm. Figures 4a and 4b show *Kp* and *Sym-H**, respectively, with the observations drawn with thick light blue lines and the SWMF simulations with thinner lines (SWMFa in blue, SWMFb in orange, and SWMFc in green). *Sym-H** is computed from the *Sym-H* index by applying a correction for solar wind dynamic pressure p_{dyn} using the same formula as the *Dst* * index given in Burton et al. (1975). This correction removes the contribution of the magnetopause current to *Sym-H*. Figure 4c shows the absolute value of the AACGM magnetic latitude at which each IB was observed. Observations from the equatorward boundary of the IB (abbreviated as LL for low latitude) are shown in blue, while observations from the poleward boundary of the IB (abbreviated as HL for high latitude) are shown in red. The two boundaries are identified according to the procedure from Dubyagin et al. (2018), as discussed in the previous section. Figure 4d shows the MLT of each IB observation, with red and blue markers identifying the HL and LL IB observations as in Figure 4c.

Figure 4e shows the maximum distance from the Earth along the field line traced from each of these IB observations, which as discussed earlier is used to estimate the current sheet crossing location. The points in Figure 4e include both the HL and the LL sets. The results for each SWMF simulation are shown, with SWMFa depicted as blue circles, SWMFb as orange squares, and SWMFc as green triangles. Figure 4f shows the values of K obtained from the MHD solution at the locations depicted in Figure 4e.

From Figure 4a that the simulated Kp is generally within 1 Kp unit of the observations, except for a Kp of zero computed at the beginning of the simulations, an early increase in Kp three hours before the storm begins and a decrease in Kp reported by SWMFc near the end of the storm. Figure 4b shows that the simulated $Sym\text{-}H^*$ values are generally within 20 nT of the observed $Sym\text{-}H^*$, with exceptions being an overestimation (in magnitude) of $Sym\text{-}H^*$ during some of the stronger periods of the storm, and an underestimation (in magnitude) of $Sym\text{-}H^*$ by SWMFc near the end of the storm.

From Figure 4c it is apparent that the IB latitude varies over time during the storm. The few quiet time IB observations are spaced fairly close together in latitude, and their latitude gradually increases from around 63 to 66 degrees between 0300 and 0800 UT. When the storm commences around 0900 UT, the IB latitude sharply decreases to around 62°. Sixty-two degrees remains the most common latitude for the next several hours, but outlier IB observations occur as high as 73°. After 2000 UT, the number and severity of HL outliers decreases somewhat, and the lower latitude limit of IB observations initially decreases to 60° around 2400 UT on 5 April, then increases gradually until reaching 64° around 1200 UT on 6 April.

Figure 4d shows that there are distinct trends in MLT over time as well. These trends are due mainly to the orbital motion of the conjugate satellites over time. Since IB latitude is known to vary with MLT (e.g., Asikainen et al., 2010; Dubyagin et al., 2018; Ganushkina et al., 2005; Lvova et al., 2005), these variations in MLT are probably responsible for some of the variations in IB latitude seen in Figure 4c.

The distances in Figure 4e reflect the latitudes shown in Figure 4c: The distances tend to increase when the IB latitudes increase and decrease when the IB latitudes decrease. This correspondence between latitude and mapping distance is expected. For a dipole field, distance increases monotonically with increasing latitude of field line foot points, and the stretched geometry of the nightside magnetosphere results in an even faster increase. A similar correspondence with latitude can be seen in Figure 4f, but the behavior is reversed, with the K estimates tending to decrease with increasing IB latitude.

The overall range of K estimations from the SWMF simulations is shown in the first two rows of Table 1, which shows the total number of usable K estimations in each row, 25th percentile, median, and 75th percentile of the K estimations. Results from all three SWMF simulations are combined together in Table 1, and only usable K estimates are included (those for which the traced field line was closed, and K was greater than 0.01). The percentiles for $K = 8$ and $K = 13$ (i.e., the percentage of K values falling below $K = 8$ and $K = 13$) are also shown. The number of K estimates falling below these thresholds provides an estimate for what percentage of the IB's might have been formed by CSS. By using two different thresholds, we are able to provide a rough estimate of the uncertainty range for this percentage. The $K_{crit} = 8$ threshold, as discussed in section 1, was originally introduced by Sergeev et al. (1983) as a rough estimate of the threshold condition for CSS and has been widely adopted by other researchers. In the present work, we adopt $K = 8$ as a probable low end of the uncertainty range for K_{crit}. For the upper end, we note that Sergeev, Chernyaeva, Angelopoulos, et al. (2015) found differences in the properties of IB's above and below $K = 13$, while Dubyagin et al. (2018) found that $4.5 < K < 13$ fell within 1 R_E of where $K = 8$ for 90% of field configurations produced by the TS05 model, and Haiducek et al. (2019) obtained corrected K values falling mostly below $K = 11$ for carefully chosen IB observations in quiet conditions. Based on these results, we have adopted $K = 13$ as an approximate upper end of the uncertainty range for K_{crit}. The results in Table 1 are separated according to whether they were obtained from observations of the HL or LL boundary of the IB. Both the medians and the interquartile ranges of K are somewhat higher for the LL set, consistent with the tendency noted in the previous paragraph that increases in IB latitude are associated with decreases in K and vice versa. The remaining rows of Table 1 will be discussed later in the paper.

Table 1
*Values Summarizing the Distribution of K and K**

Model type	IB set	*n*	25th percentile	Median	75th percentile	$K \leq 8$ percentage	$K \leq 13$ percentage	*y* axis intercept	Intercept 95% CI
Uncorrected K									
SWMF	HL	254	8.18	16.7	30.9	23.6	38.6	—	—
SWMF	LL	339	9.69	18.9	33.1	20.1	35.1	—	—
Empirical	HL	254	3.93	10.3	15.9	40.2	61.4	—	—
Empirical	LL	273	6.01	12.3	20.0	31.5	52.7	—	—
Both	HL	508	6.32	13.0	22.4	31.9	50.0	—	—
Both	LL	612	7.98	15.4	27.9	25.2	43.0	—	—
K correction*									
SWMF	HL	254	7.21	12.8	20.3	29.1	51.6	11.5	[10.3, 12.8]
SWMF	LL	339	8.26	14.9	24.6	23.3	42.2	13.6	[12.4, 14.9]
Empirical	HL	254	4.99	9.61	15.7	42.5	66.1	7.87	[7.01, 8.83]
Empirical	LL	273	6.95	12.7	19.3	31.1	51.3	10.7	[9.54, 11.9]
Both	HL	508	5.61	10.8	17.1	36.4	59.4	9.35	[8.62, 10.1]
Both	LL	612	7.54	13.8	21.5	27.3	46.2	12.1	[11.3, 13.0]

Note. SWMF = Space Weather Modeling Framework; HL = high-latitude; LL = low-latitude; IB = isotropic boundary.

The negative correlation between the estimated K in the IB formation region and IB latitude can be explained by both the EMIC wave and the CSS mechanisms, noting that the value of K can be approximated as

$$K = \frac{R_c}{r_g} \approx \frac{qB_z^2}{\sqrt{2mE}\mathrm{d}B_r/\mathrm{d}z}, \tag{2}$$

where q denotes the particle charge, m the particle mass, and E the particle energy. B_r is the radial component of magnetic field in GSM coordinates, given by

$$B_r = \frac{xB_x + yB_y}{\sqrt{x^2 + y^2}}. \tag{3}$$

B_z near the equatorial plane decreases as $\frac{1}{r^3}$ in a dipole field, and the stretched field lines in the nightside magnetosphere result in even faster decrease. This tends to result in an inverse relationship where K decreases with increasing distance. If the IB formation process is independent of K (as is the case for EMIC wave scattering), the IB latitude roughly corresponds to the distance of the IB field line in the equatorial plane, resulting in a negative correlation between IB latitude and K. For CSS-driven IB formation, this relationship between K and distance from the Earth should be absent since we are computing K at points mapped from the IB, and IB formation through CSS is directly controlled by K. However, if the simulation fails to respond to fast variations in the magnetosphere, the IB will be projected to (and K estimated at) points distributed around the true IB formation region, and the deviation of the model K estimates from reality will reflect the average radial profile of K, with associated negative correlation between K and IB latitude. Thus, the approximately inverse relationship between K and distance seen in Figures 4e and 4f could indicate a failure of the model to reproduce the true magnetic field geometry, or it could indicate that some of the observed IB's were formed by EMIC scattering.

Noting the quadratic dependence of K on B_z in equation (2), we estimate the error in B_z at the locations were K was estimated by computing the B_z errors at the spacecraft that are conjugate with each IB location. The conjugate spacecraft include at least one and in some cases several of the GOES and THEMIS satellites. We denote the averaged error as $\overline{\Delta B_z}$. Figure 5 shows K as a function of $\overline{\Delta B_z}$ for the points from Figure 4. Figure 5a shows the HL points, while Figure 5b shows the LL points. Results from each model run are depicted using the same color and marker scheme as Figure 4. Fit lines are drawn in black on top of the points. Note that a logarithmic scale is used for the y axis and a linear fit has been performed on the transformed data; the reason for this will be explained later. Points that mapped to within 8 R_E of the MHD domain boundaries have been excluded.

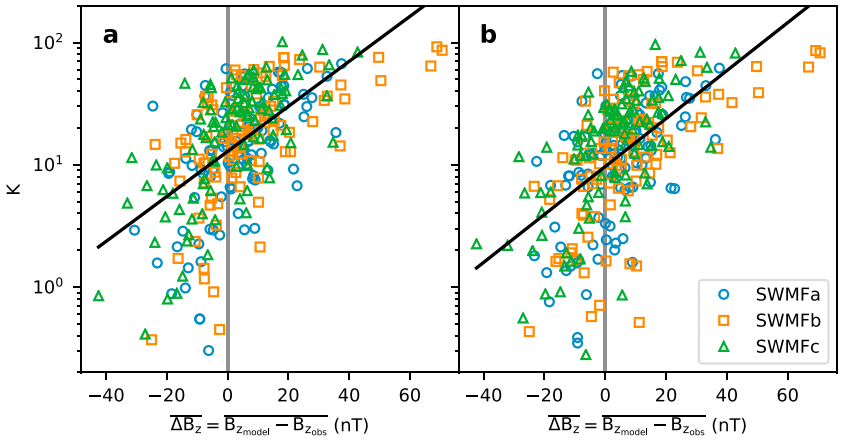

Figure 5. K as a function of $\overline{\Delta B_z}$ for all three magnetohydrodynamic simulations, computed for locations mapped from isotropic boundary observations in the high-latitude data set (a) and the low-latitude data set (b). Black lines show linear fits (in log space) to the data.

Figure 5 shows that K increases with increasing $\overline{\Delta B_z}$. Noting the quadratic dependence of K on B_z in equation (2), K at the IB location will be overestimated if the model overestimates B_z. In addition, this effect is strengthened by the mapping error, because understretched model fields map the IB field line closer to the Earth, in the region of higher K.

From Figure 5 it appears that the SWMF has a tendency to overpredict B_z, with a substantial fraction of the ΔB_z values falling between 0 and 20 nT. Indeed, we found that the SWMF simulations overestimated $\overline{\Delta B_z}$ about 65–70% of the time (more detailed statistics for $\overline{\Delta B_z}$ are given in Table S2 in the supporting information). Most of the K values corresponding to $\overline{\Delta B_z} > 0$ fall within the interquartile ranges shown in the first two rows of Table 1. Anomalously low K values ($K \lesssim 4$) appear only when $\overline{\Delta B_z} \lesssim 12$. Despite the correlation between K and ΔB_z, K values seem to be constrained to $K \lesssim 100$, with K remaining below that threshold even for the largest overestimations of B_z.

6. Empirical Results

In this work we use the empirical magnetic field models T01, TS05, and TA16. All three are available at the website (http://geo.phys.spbu.ru/tsyganenko/modeling.html). These models operate by computing a sum of analytical functions of a set of solar wind and geomagnetic activity parameters. In the case of T01 and TS05 these functions represent specific current systems, while in TA16 they are radial basis functions with no correspondence among the known current systems in the magnetosphere.

We now describe some of the features of these models that are relevant to estimating K. In the T01 model, the current sheet thickness is constant, but the inner edge of the tail current moves earthward with increasing activity, and the tail current radial profile is controlled by two independent submodules.

The TS05 model was designed specifically to model storm time conditions, and it was constructed by fitting to data from storm periods. The position and thickness of the TS05 tail current vary with activity and are parameterized by a complex integral functions of the time history of solar wind parameters.

While the T01 and TS05 models used predetermined functions to define the magnetospheric current systems, the TA16 model replaces these ad hoc functions with a sum of radial basis functions controlled by driving parameters (Newell et al., 2007). This avoids imposing assumptions about the form of the current systems through the choice of fitting functions. However, the limited number of observations available for fitting precludes resolving fine spatial structures by this method.

We traced field lines from the IB locations (in AACGM coordinates) using each of these models, and with a dipole representation for intrinsic field of the Earth. Geopack was used to perform the actual tracing of the field lines. As with the SWMF simulations, $K = \frac{R_c}{r_g}$ was estimated at the point of maximum distance from the Earth along each field line, using the detector cutoff energies (Table S1 in the supporting information) to

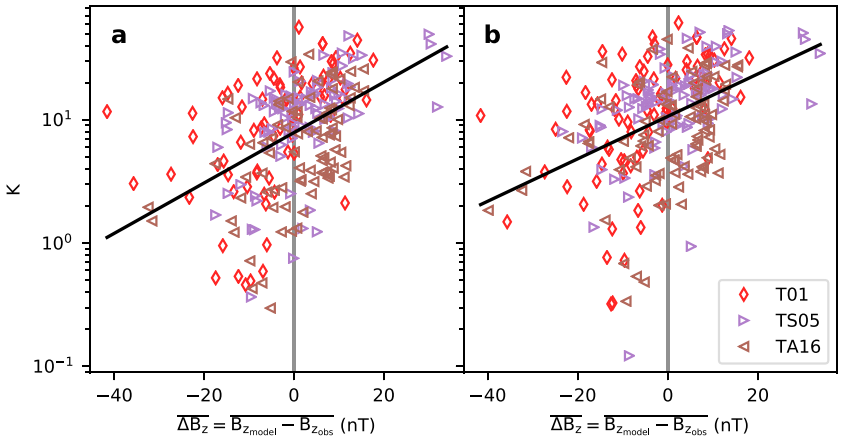

Figure 6. K as a function of $\overline{\Delta B_z}$ for the empirical models, computed for locations mapped from isotropic boundary observations in the high-latitude data set (a) and low-latitude data set (b). The black lines show a linear fit (in log space) to the data.

estimate r_g and equation (1) to estimate R_c. The output from the models was also computed at the locations of the THEMIS spacecraft for comparison with observations.

Figure 6 shows the K values obtained from the empirical models as a function of $\overline{\Delta B_z}$, which as with the SWMF simulations represents the model error in B_z, averaged over the THEMIS spacecraft that were conjugate with each IB observation. Points from T01 are shown as red diamonds, TS05 as purple right-pointing triangles, and TA16 as brown left-pointing triangles. Figure 6a shows the HL data, and Figure 6b shows the LL data. A least squares fit (in log space) through all the points is shown in black. It appears that the three models performed similarly, and a general similarity with the SWMF simulations is also apparent, although the K values are somewhat lower and the tendency to overestimate B_z is less pronounced.

From Figure 6 it is also apparent that the T01 model has a tendency toward underestimation of $\overline{\Delta B_z}$, while the TS05 and TA16 models tend toward overestimation of $\overline{\Delta B_z}$. This is further supported by the metrics for $\overline{\Delta B_z}$ given in Table S2 of the supporting information.

The third and fourth rows of Table 1 summarize the range of K obtained from the empirical models. As with the SWMF results, the empirical model results in the table were obtained by combining the results from all the empirical models together. K estimates below 0.01 were excluded from the results. Like the SWMF estimates of K, the median, 25th, and 75th percentiles are all higher for the LL data set than for the HL data set. K values at all three quartiles are lower than they are for SWMF, indicating a systematic tendency toward lower K values with the empirical models. On the other hand, the interquartile ranges overlap substantially between the two classes of models.

7. K Correction

We have seen that both the SWMF simulations and the empirical models have tendencies to overestimate or underestimate B_z relative to in situ observations in the magnetotail. However, both the SWMF simulations and the empirical models exhibit a positive correlation between K and $\overline{\Delta B_z}$, which is consistent with the quadratic relationship between K and B_z seen in equation (2). This relationship enables us to correct the model-derived K values for the known errors in B_z, using the correction procedure previously described in Dubyagin et al. (2018) and Haiducek et al. (2019). The procedure consists of taking the logarithm of both sides of equation (2) then linearizing to obtain a linear equation of the form

$$\log K = A_1 + A_2 \overline{\Delta B_z}, \tag{4}$$

where A_1 and A_2 are obtained from the fit line shown in Figures 5 and 6. From this we obtain a corrected value K^*, which estimates the value K would have in the absence of B_z errors and is given by

$$K^* = K \exp(-A_2 \overline{\Delta B_z}). \tag{5}$$

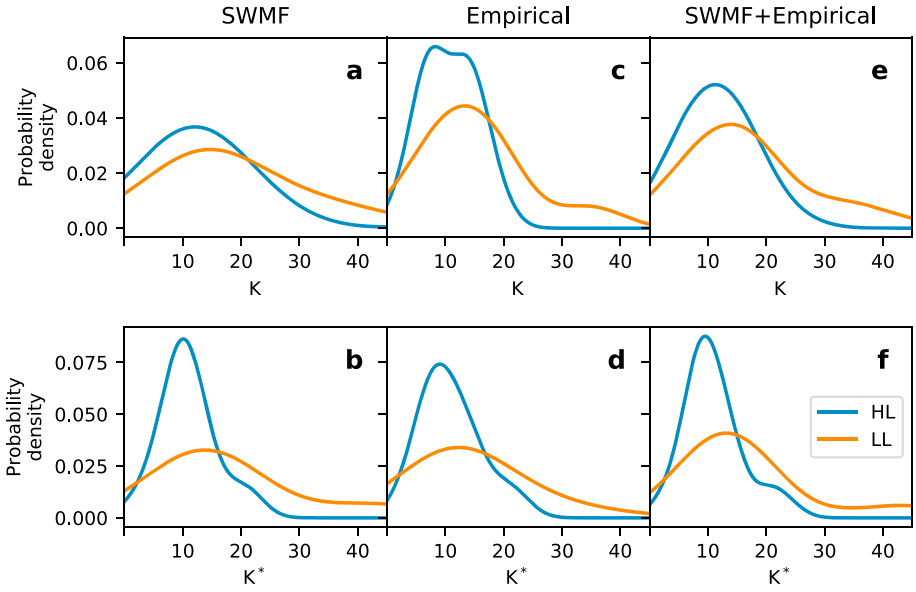

Figure 7. Distributions of (a) K and (b) K^* for all three magnetohydrodynamic simulations, and distributions of (c) K and (d) K^* for all empirical models. (e and f) Space Weather Modeling Framework (SWMF) and empirical models together. The distributions have been separated according to whether the observations came from the high-latitude (HL) or the low-latitude (LL) edge of the isotropic boundary.

The lower half of Table 1 shows statistics for K^*. As with the K results, data are shown for the SWMF simulations, empirical models, and both together. Each is further broken down into results for the HL and LL IB observations. For K^*, the y axis intercept from the fit of equation (4) is also given, along with its 95% confidence interval. The intercepts provide an estimation of what the average value of K would be in the case of zero magnetic field error.

From the values in Table 1, it is apparent that the SWMF tends to produce higher values of K (as indicated by the higher median and interquartile ranges) compared with the empirical models. The K^* correction tends to produce smaller values compared with the uncorrected K values while also reducing the amount of difference between the SWMF and the empirical model results compared with K.

The values in Table 1 also show that the LL IB observations tended to be associated with larger values of K and K^* compared with the HL observations. Each of the rows of the table showing data from the LL set has a higher median than the corresponding row from the HL set. For instance, the SWMF K estimations for the HL set have a median of 10.7, while those from the LL set have a median of 11.0. Similarly, the empirical model estimations for the HL set have a median of 10.8, while those for the LL set have a median of 14.3. This is consistent with the expected relationship between K and latitude discussed earlier.

The $K = 8$ and $K = 13$ percentiles in Table 1 provide an estimate of what fraction of the IB observations might have been produced by CSS (for which $K \lesssim 8$–13 is expected). The remaining IB observations (those for which $K \gtrsim 8$–13) could potentially be the result of EMIC wave interactions. For SWMF, 23.6% of the uncorrected HL K values fall below $K = 8$, and 38.6% fall below $K = 13$; for the LL set it is 20.1% and 35.1%. For the empirical models 40.2% of the values from the HL set are below $K = 8$ and 61.4% are below $K = 13$, while for the LL set it is 31.5% and 52.7%. The K^* correction increases the number of SWMF estimates that fall below the $K = 8$ and $K = 13$ thresholds, to 29.1% and 51.6%, respectively, for the HL set, and 23.3% and 42.2%, respectively, for the LL set. The K^* correction has a somewhat less significant effect on the empirical model results, with the percentages below the $K = 8$ and $K = 13$ falling within 5% compared with the uncorrected K.

Figure 7 shows the distributions of K before and after correction, represented using kernel density estimation (Parzen, 1962). A kernel density estimation approximates a probability density function by convolving a set of discrete points with a Gaussian kernel. The resulting plot can be interpreted in much the same way as a normalized histogram. The HL IB data are shown in blue, and LL IB data are shown in orange.

Figure 7a shows the distribution of K values estimated by SWMF, while Figure 7b shows the corresponding distribution of K^*. Figures 7c and 7d show K and K^* for the empirical models, while Figures 7e and 7f show the results of combining the SWMF and empirical results into a single data set and computing K^* for the combined data set.

The empirical models (Figure 7c) produce slightly narrower distributions of K compared with SWMF (Figure 7a), but after correction the distributions become more comparable, and the SWMF distribution of K^* for the HL set (Figure 7b) is slightly narrower than that of the empirical models (Figure 7d). For both classes of models, the K^* correction (Figures 7b, 7d, and 7f) produces a narrower distribution for the HL set compared with the uncorrected K values (Figures 7a, 7c, and 7e). However, for the LL set the opposite is true, with the SWMF distribution being relatively unaffected and the empirical distribution being widened appreciably. In all the distributions of Figure 7, a noticeable difference can be seen between the LL and HL data. For values of K and K^* greater than about 20, the probability density is higher for the LL set than for the HL set, while for values less than this, the probability density is higher for the HL set than for the LL set. This means that the LL points tend to be associated with higher values of K. This is consistent with the tendency previously noted in Table 1. When the K^* correction (Figures 7b, 7d, and 7f) is applied, the same pattern is seen that LL observations are associated with higher values, and the effect is more pronounced for the corrected values.

8. Discussion

The goal of this study is to test what fraction of observed IB's during the storm on 4–6 April 2010 may have been the result of CSS. To accomplish this, we estimated $K = \frac{R_c}{r_g}$ associated with ion IB observations. K provides a measure of the effectiveness of the CSS process at a particular location. We used MHD and empirical models to trace field lines from the IB observation locations to the magnetotail and to estimate K where those field lines cross the current sheet. We then corrected our K estimations for errors in the model magnetic fields that could be quantified with in situ observations from spacecraft in the magnetotail. By correcting for these errors, and by using of multiple models to estimate K, we are able to constrain the possible range of K. This is the first study to explore IB properties using an MHD model during storm conditions.

A number of previous studies have noted a tendency for SWMF to produce understretched magnetic fields on the nightside. As discussed in section 5, this is expected to result in overestimation of K. Glocer et al. (2009) found that SWMF overestimated B_z at GOES spacecraft during a storms on 4 May 1998 and 31 March 2001, though they also found that this could be improved by coupling a wind model to Block Adaptive Tree Solar-Wind, Roe-type Upwind Scheme. Ganushkina et al. (2010) showed that SWMF overestimated B_z at GOES spacecraft during storms on 6–7 November 1997 and 21–23 October 1998. Ilie et al. (2015) reported overprediction at GOES, Geotail, and THEMIS spacecraft during a quiet interval on 13 February 2009, and Haiducek et al. (2019) reported this for different simulations of the same event. In the present study we find this tendency as well, with all three simulations overestimating B_z for about 65–70% of the IB observations.

The amount of tail stretching in TA16 was previously reported to be similar to the older T89 model (Tsyganenko & Andreeva, 2016), which in turn has been reported as producing overstretched fields in the magnetotail (Peredo et al., 1993; Tsyganenko, 1989). Haiducek et al. (2019) reported understretched fields for T01 and overstretched fields in TS05 and TA16. Results in the present work show a slight tendency toward overstretching in T01, but a slight tendency toward understretching in TS05 and TA16, based on errors in B_z relative to in situ observations.

Compared with SWMF, the empirical models tend to produce smaller values of K, consistent with the tendency noted above of understretched fields in SWMF and overstretched fields in the empirical models. However, the distributions of K overlap significantly between the two classes of models even before correction. The median K values and percentiles in Table 1 demonstrate that, after correction, the difference between the distributions of K obtained using MHD and those obtained using the empirical models is less than the difference between the K distributions found by using different criteria of IB selection (HL or LL data sets). This is different from the quiet time results of Haiducek et al. (2019), which included nonoverlapping distributions of uncorrected K, with the empirical models tending toward quite small values of K and the SWMF K values uniformly above 10. The overlapping distributions reflect the presence of much higher K estimates (on average) coming from the empirical models compared with Haiducek et al. (2019), along with marginally lower K estimates from SWMF and broader distributions for both classes of models.

The broader distributions are probably the result of using less restrictive selection criteria for the IB observations, as well as storm time variability. Storm conditions likely increase the range of K estimates both by causing the true value of K to vary more broadly (due to EMIC scattering, as well as producing CSS under a wider variety of conditions). Storm conditions also create rapidly varying dynamics which the models are not always able to reproduce, contributing to errors in magnetic field configuration and causing randomly varying errors in K.

The results of our study are somewhat different from those obtained by Dubyagin et al. (2018) using the TS05 model in the 21–03 MLT sector for larger statistics (nine storms, >200 IB observations). Dubyagin et al. (2018) found that 68% of the events in their HL data set had $K^* < 13$, which is reasonably close to the 66.1% obtained from the HL data set using empirical models in our study. However, 63% of their LL IB's had $K^* < 13$, which is significantly higher than the 51.3% in our LL data set (see Table 1). In both cases the percentages are lower. When the SWMF results are added, the percentages decrease further since SWMF tends to produce higher values for K and K^*. Finally, using a $K^* < 8$ threshold condition reduces the percentages further. The lower percentages we obtained compared to Dubyagin et al. (2018) can be attributed to several factors including

1. A different methodology for estimating the uncertainty (the use of two K thresholds versus a single one)
2. The use of multiple models (three empirical models, plus three MHD simulations) in the present work, compared with a single empirical model in Dubyagin et al. (2018)
3. The application of additional restrictions on MLT and ΔB_z by Dubyagin et al. (2018)
4. Differences in the magnetospheric state between the storm we analyzed and those analyzed in Dubyagin et al. (2018)

Given the differences in the analysis, and in the events included in the two studies, our paper and Dubyagin et al. (2018) should be considered complementary, but some caution should be applied when making quantitative comparisons between the two.

The results in Haiducek et al. (2019) made it clear that errors in the magnetic field models can affect K values significantly, but also that such errors, if quantified, can be corrected for effectively. However, it should be noted that the corrections provide only a rough estimate of the true value of K. These corrections are subject to a number of sources of uncertainty, including errors due to the linearization of the expression for K, the position of satellites relative to where K is actually estimated, and the fact that our correction procedure involves a fit to numerous K estimates from numerous IB observations, each of which came from a different time, with a different magnetospheric state and different satellite positions for each. By fitting all of these points together we find the average relationship between the magnetic field errors and K estimates. The true relationship between the two probably varies with the magnetospheric state and the satellite positions, which our correction procedure does not account for. With the ΔB_z estimates there is a potential issue with the GOES magnetometer data in that it may contain offsets of unknown magnitude (Singer et al., 1996).

Despite these sources of uncertainty, there are indications that the correction procedure is successful in removing much of the difference between the two classes of models. The distributions of K become narrower and substantially more similar to each other after correction. While we have no ground-truth measurement with which to test our K estimations, we interpret the similarity between the distributions of K obtained by very different types of models as a sign that both are likely reproducing the major characteristics of the true K distribution. On the other hand, we also noted in section 7 that the correction procedure seems to amplify the differences between the HL and LL data sets. This is largely due to the correction procedure narrowing the distribution of K obtained from the HL IB observations, while the distribution of K derived from the LL data is relatively unchanged. This could indicate that the LL data are subject to greater inaccuracies in the ΔB_z estimates used in the correction or that the LL data are more sensitive to additional error terms not included in the correction procedure. Another possibility is that variance in the incident particle population prior to scattering plays a greater role for the particles observed at the LL latitudes. Finally, it is possible that the procedure used to identify the HL and LL locations is somehow more precise for the HL latitudes.

In addition to checking the K values to determine whether they are below a given threshold value, we can also check for a dependence on MLT as an indication of whether CSS is the mechanism responsible for IB formation. EMIC scattering has been noted to contribute significantly to proton precipitation in the dusk sector (e.g., Fuselier, 2004; Yahnin & Yahnina, 2007; Zhang et al., 2008). A number of previous studies have

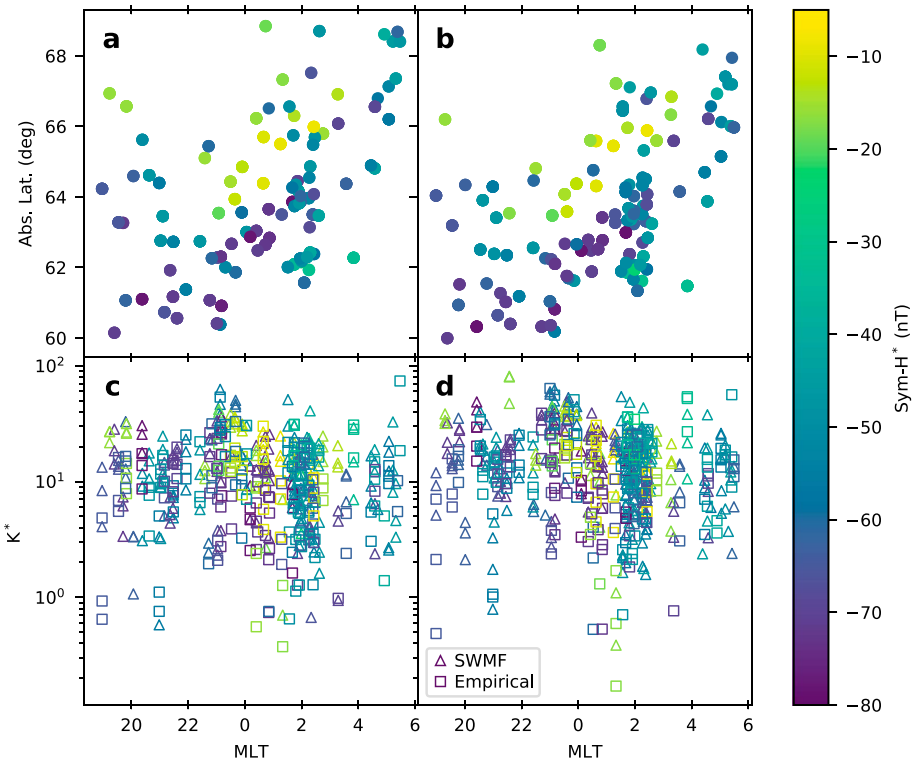

Figure 8. (a) HL IB latitude as a function of MLT, (b) LL IB latitude as a function of MLT, (c) HL K^* as a function of MLT, (d) LL K^* as a function of MLT. All points are colored by *Sym-H**. Shapes in (c) and (d) denote the class of model (SWMF or empirical). SWMF = Space Weather Modeling Framework; HL = high-latitude; LL = low-latitude; IB = isotropic boundary; MLT = magnetic local time.

found a noon-midnight asymmetry in IB latitude, characterized by a nightside minimum latitude and a dayside maximum latitude (e.g., Asikainen et al., 2010; Ganushkina et al., 2005; Sergeev et al., 1993; Yue et al., 2014). In addition, many studies have found a tendency for IB latitude to decrease as *Sym-H* becomes more negative (e.g., Asikainen et al., 2010; Dubyagin et al., 2018; Hauge & Söraas, 1975; Ganushkina et al., 2005; Lvova et al., 2005; Søraas et al., 2002). In most cases the noon-midnight asymmetry in latitude is accompanied by a weaker dawn-dusk asymmetry, with the minimum IB latitude occurring around 23 MLT (e.g., Asikainen et al., 2010; Ganushkina et al., 2005; Lvova et al., 2005; Newell et al., 1998; Sergeev et al., 1997; Yue et al., 2014). Figures 8a and 8b show the latitude of our IB observations as a function of MLT, with the HL data set shown in Figure 8a and the LL data set in 8b. As has been seen by previous authors, the minimum IB latitude occurs in the premidnight sector, and a dawn-dusk asymmetry is clearly visible. A correlation with *Sym-H* is also apparent. Figures 8c and 8d show K^* as a function of MLT, with the HL data in Figure 8c and the LL data in Figure 8d. All plots of Figure 8 are colored by *Sym-H**, and SWMF results are plotted with triangles while empirical models are plotted with squares. Figure 8 shows that K^* exhibits none of the trends found in the IB latitude, which is consistent with CSS playing a significant role in IB formation since it suggests that K is controlling the pitch angle scattering rather than some other process. Note, however, that the MLT dependence shown in Figure 8 is affected by the motions of the GOES and THEMIS satellites since we use only IB observations that are conjugate with those spacecraft. It should be noted that independence of the K parameter on MLT was also found by Dubyagin et al. (2018) using only empirical models. However, that study concentrated on a narrower MLT sector (21–03 MLT), and there were serious doubts that this dependence would not emerge if 18–21 MLT sector was included. Indeed, the plasmaspheric plume is often seen at ≈18 MLT and the EMIC wave related precipitations have also been detected in this sector (Yahnin & Yahnina, 2007).

The independence of K^* on MLT, despite a dependence of IB latitude on MLT, was interpreted by Dubyagin et al. (2018) as an indication that the CSS was the operative scattering mechanism for a majority of their data. Our results also find K^* to be independent of MLT, even though a lower percentage of our K^* values were

within the expected range for CSS. We conducted additional tests in which we plotted K^* as a function of MLT while limiting the data set to IB observations for which K^* exceeded a specified threshold. By doing so, we found that K^* is independent of MLT even when $K^* > 30$. This could indicate that the lack of dependence of K^* is not due to K controlling the scattering process but is simply the result of random variations in the estimated K values due to mapping errors which are large enough to obscure the MLT dependence. If this is the case, then the mapping accuracy must be increased before the dependence of K on MLT can be used reliably as an indicator of CSS, and comparison of K with a threshold value is probably the better criterion.

The conclusions of the paper can be summarized as follows:

1. By correcting each K estimate using in situ observations from 2–3 conjugate satellites in the current sheet, we were able to produce consistent results, with similar distributions of K obtained using both empirical and MHD models.
2. Accounting for uncertainty in the IB latitude and in the threshold condition for K, we find that between 29% and 54% of the IB observations may be the result of CSS.
3. We find that K^* is independent of both $Sym\text{-}H^*$ and MLT during this storm interval, and this independence persists even for high K values.

Acknowledgments
The NOAA/POES particle data were downloaded from the National Geophysical Data Center website (https://www.ngdc.noaa.gov/stp/satellite/poes/index.html). Thanks to Howard Singer for providing the GOES magnetometer data. The magnetometer data (in spacecraft coordinates) can be found online (https://satdat.ngdc.noaa.gov/sem/goes/data/avg/). GOES magnetometer data in GSM coordinates are included in the supporting information. THEMIS data were retrieved using the THEMIS Data Analysis Software (TDAS; http://themis.igpp.ucla.edu/software.shtml). We acknowledge NASA contract NAS5-02099 and V. Angelopoulos for use of data from the THEMIS Mission, specifically, K. H. Glassmeier, U. Auster, and W. Baumjohann for the use of FGM data provided under the lead of the Technical University of Braunschweig and with financial support through the German Ministry for Economy and Technology and the German Center for Aviation and Space (DLR) under contract 50 OC 0302 and C. W. Carlson and J. P. McFadden for use of ESA data. The research of S. Dubyagin and N. Ganushkina leading to these results was partly funded by the European Union's Horizon 2020 research and innovation programme under grant agreement 637302 PROGRESS. The work at the University of Michigan was also partly funded by the National Aeronautics and Space Administration under grant agreements NNX14AF34G, NNX17AB87G, and 80NSS17K0015 issued through the ROSES-2013 and ROSES-2016 programmes and by the National Science Foundation under grant agreement 1663770. Part of the results presented here has been achieved under the framework of the Finnish Centre of Excellence in Research of Sustainable Space (FORESAIL) funded by the Academy of Finland, decision number 312351. Portions of the work of J. Haiducek leading to these results were performed while he held a National Research Council (NRC) Research Associateship award at the U.S. Naval Research Laboratory. Portions of the work of J. Haiducek leading to these results were financially supported by the U.S. Veterans administration under the Post-9/11 GI Bill. The Spacepy python library (Burrell et al., 2018; Morley et al., 2011, 2014) was used for a number of tasks related to reading and analyzing data in this paper.

References

Alfvén, H., & Fälthammar, C. G. (1963). *Cosmical electrodynamics: Fundamental principles*, International series of monographs on physics (Vol. 1). Oxford, UK: Clarendon Press. https://doi.org/10.1029/2010JA015774

Asikainen, T., Maliniemi, V., & Mursula, K. (2010). Modeling the contributions of ring, tail, and magnetopause currents to the corrected Dst index. *Journal of Geophysical Research*, *115*, A12203. https://doi.org/10.1029/2010JA015774

Asikainen, T., Mursula, K., & Maliniemi, V. (2012). Correction of detector noise and recalibration of NOAA/MEPED energetic proton fluxes. *Journal of Geophysical Research*, *117*, A09204. https://doi.org/10.1029/2012JA017593

Auster, H. U., Glassmeier, K. H., Magnes, W., Aydogar, O., Baumjohann, W., Constantinescu, D., et al. (2008). The THEMIS fluxgate magnetometer. *Space Science Reviews*, *141*(1–4), 235–264. https://doi.org/10.1007/s11214-008-9365-9

Baker, K. B., & Wing, S. (1989). A new magnetic coordinate system for conjugate studies at high latitudes. *Journal of Geophysical Research*, *94*(A7), 9139–9143. https://doi.org/10.1029/JA094IA07P09139

Brambles, O. J., Lotko, W., Zhang, B., Ouellette, J., Lyon, J., & Wiltberger, M. (2013). The effects of ionospheric outflow on IC ME and SIR driven sawtooth events. *Journal of Geophysical Research: Space Physics*, *118*, 6026–6041. https://doi.org/10.1002/JGRA.50522

Brambles, O. J., Lotko, W., Zhang, B., Wiltberger, M., Lyon, J., & Strangeway, R. J. (2011). Magnetosphere sawtooth oscillations induced by ionospheric outflow. *Science*, *332*(6034), 1183–1186. https://doi.org/10.1126/science.1202869

Büchner, J., & Zelenyi, L. M. (1987). Chaotization of the electron motion as the cause of an internal magnetotail instability and substorm onset. *Journal of Geophysical Research*, *92*(A12), 13,456–13,466. https://doi.org/10.1029/JA092iA12p13456

Burrell, A. G., Halford, A. J., Klenzing, J., Stoneback, R. A., Morley, S. K., Annex, A. M., et al. (2018). Snakes on a spaceship—An overview of Python in heliophysics. *Journal of Geophysical Research: Space Physics*, *123*, 10,384–10,402. https://doi.org/10.1029/2018JA025877

Burton, R. K., McPherron, R. L., & Russell, C. T. (1975). An empirical relationship between interplanetary conditions and Dst. *Journal of Geophysical Research*, *80*(31), 4204–4214. https://doi.org/10.1029/JA080i031p04204

Daglis, I. A. (1997). The role of magnetosphere-ionosphere coupling in magnetic storm dynamics, *Magnetic storms* (pp. 107–116). Washington, DC: American Geophysical Union (AGU). http://doi./10.1029/GM098p0107

DeZeeuw, D. L., Gombosi, T. I., Groth, C. P. T., Powell, K. G., & Stout, Q. F. (2000). An adaptive MHD method for global space weather simulations. *IEEE Transactions on Plasma Science*, *28*(6), 1956–1965.

Delcourt, DC, Malova, HV, & Zelenyi, LM (2006). Quasi-adiabaticity in bifurcated current sheets. *Geophysical Research Letters*, *33*, L06106. https://doi.org/10.1029/2005GL025463

Delcourt, D. C., Moore, T. E., Giles, B. L., & Fok, M.-C. (2000). Quantitative modeling of modulated ion injections observed by Polar-Thermal Ion Dynamics Experiment in the cusp region. *Journal of Geophysical Research*, *105*(A11), 25,191–25,203. https://doi.org/10.1029/2000JA000034

Delcourt, D. C., Sauvaud, J.-A., Martin, R. F., & Moore, T. E. (1996). On the nonadiabatic precipitation of ions from the near-Earth plasma sheet. *Journal of Geophysical Research*, *101*(A8), 17,409–17,418. https://doi.org/10.1029/96JA01006

Dubyagin, S., Ganushkina, N., Apatenkov, S., Kubyshkina, M., Singer, H., & Liemohn, M. (2013). Geometry of duskside equatorial current during magnetic storm main phase as deduced from magnetospheric and low-altitude observations. *Annales Geophysicae*, *31*(3), 395–408. http://www.ann-geophys.net/31/395/2013/

Dubyagin, S., Ganushkina, N. Y., & Sergeev, V. (2018). Formation of 30 keV proton isotropic boundaries during geomagnetic storms. *Journal of Geophysical Research: Space Physics*, *123*, 3436–3459. https://doi.org/10.1002/2017JA024587

Erlandson, R. E., & Ukhorskiy, A. J. (2001). Observations of electromagnetic ion cyclotron waves during geomagnetic storms: Wave occurrence and pitch angle scattering. *Journal of Geophysical Research*, *106*(A3), 3883–3896.

Evans, D. S., & Greer, M. S. (2000). Polar Orbiting Environmental Satellite Space Environment Monitor-2: Instrument descriptions and archive data documentation (Tech. Rep.) Boulder, Colorado: National Oceanic and Atmospheric Administration. ftp://satdat.ngdc.noaa.gov/sem/poes/docs/sem2_docs/2006/SEM2v2.0.pdf

Fuselier, S. A. (2004). Generation of transient dayside subauroral proton precipitation. *Journal of Geophysical Research*, *109*, A12227. https://doi.org/10.1029/2004JA010393

Ganushkina, N. Y., Liemohn, M. W., Kubyshkina, M. V., Ilie, R., & Singer, H. J. (2010). Distortions of the magnetic field by storm-time current systems in Earth's magnetosphere. *Annales Geophysicae*, *28*(1), 123–140. https://doi.org/10.5194/angeo-28-123-2010

Ganushkina, N. Y., Pulkkinen, T. I., Kubyshkina, M. V., Sergeev, V. A., Lvova, E. A., Yahnina, T. A., et al. (2005). Proton isotropy boundaries as measured on mid- and low-altitude satellites. *Annales Geophysicae*, *23*(5), 1839–1847. https://doi.org/10.5194/angeo-23-1839-2005

Gilson, M. L., Raeder, J., Donovan, E., Ge, Y. S., & Kepko, L. (2012). Global simulation of proton precipitation due to field line curvature during substorms. *Journal of Geophysical Research*, *117*, A05216. https://doi.org/10.1029/2012JA017562

Glocer, A., Tóth, G., Gombosi, T., & Welling, D. (2009). Modeling ionospheric outflows and their impact on the magnetosphere, initial results. *Journal of Geophysical Research*, *114*, A05216. https://doi.org/10.1029/2009JA014053

Gvozdevsky, B. B., Sergeev, V. A., & Mursula, K. (1997). Long lasting energetic proton precipitation in the inner magnetosphere after substorms. *Journal of Geophysical Research*, *102*(A11), 24,333–24,338. https://doi.org/10.1029/97JA02062

Haiducek, J. D., Ganushkina, N. Y., Dubyagin, S., & Welling, D. T. (2019). Relating observed locations of energetic proton isotropic boundaries with magnetic field geometry during quiet times. *Journal of Geophysical Research: Space Physics*, *124*(3), 1785–1805.

Haiducek, J. D., Welling, D. T., Ganushkina, N. Y., Morley, S. K., & Ozturk, D. S. (2017). SWMF global magnetosphere simulations of January 2005: Geomagnetic indices and cross-polar cap potential. *Space Weather*, *15*, 1567–1587. https://doi.org/10.1002/2017SW001695

Halford, A. J., Fraser, B. J., & Morley, S. K. (2010). EMIC wave activity during geomagnetic storm and nonstorm periods: CRRES results. *Journal of Geophysical Research*, *115*, A12248. https://doi.org/10.1029/2010JA015716

Hauge, R., & Söraas, F. (1975). Precipitation of > 115 keV protons in the evening and forenoon sectors in relation to the magnetic activity. *Planetary and Space Science*, *23*(8), 1141–1154. https://doi.org/10.1016/0032-0633(75)90164-6

Ilie, R., Ganushkina, N., Toth, G., Dubyagin, S., & Liemohn, M. W. (2015). Testing the magnetotail configuration based on observations of low-altitude isotropic boundaries during quiet times. *Journal of Geophysical Research: Space Physics*, *120*, 10,557–10,573. https://doi.org/10.1002/2015JA021858

Imhof, W. L., Reagan, J. B., & Gaines, E. E. (1977). Fine-scale spatial structure in the pitch angle distributions of energetic particles near the midnight trapping boundary. *Journal of Geophysical Research*, *82*(32), 5215–5221. https://doi.org/10.1029/JA082i032p05215

Kennel, C. F., & Petschek, H. E. (1966). Limit on stably trapped particle fluxes. *Journal of Geophysical Research*, *71*(1), 1–28. https://doi.org/10.1029/JZ071i001p00001

Liang, J., Donovan, E., Ni, B., Yue, C., Jiang, F., & Angelopoulos, V. (2014). On an energy-latitude dispersion pattern of ion precipitation potentially associated with magnetospheric EMIC waves. *Journal of Geophysical Research: Space Physics*, *119*, 8137–8160. https://doi.org/10.1002/2014JA020226

Liu, Y., Luhmann, J. G., Bale, S. D., & Lin, R. P. (2011). Solar source and heliospheric consequences of the 2010 April 3 coronal mass ejection: A comprehensive view. *The Astrophysical Journal*, *734*(2), 84. https://doi.org/10.1088/0004-637X/734/2/84

Lvova, E. A., Sergeev, V. A., & Bagautdinova, G. R. (2005). Statistical study of the proton isotropy boundary. *Annales Geophysicae*, *23*, 1311–1316. https://hal-insu.archives-ouvertes.fr/file/index/docid/317716/filename/angeo-23-1311-2005.pdf

Möstl, C., Temmer, M., Rollett, T., Farrugia, C. J., Liu, Y., Veronig, A. M., et al. (2010). STEREO and Wind observations of a fast ICME flank triggering a prolonged geomagnetic storm on 5-7 April 2010. *Geophysical Research Letters*, *37*, L24103. https://doi.org/10.1029/2010GL045175

McFadden, J. P., Carlson, C. W., Larson, D., Bonnell, J., Mozer, F., Angelopoulos, V., et al. (2008). THEMIS ESA first science results and performance issues. *Space Science Reviews*, *141*(1–4), 477–508. https://doi.org/10.1007/s11214-008-9433-1

McFadden, J. P., Carlson, C. W., Larson, D., Ludlam, M., Abiad, R., Elliott, B., et al. (2008). The THEMIS ESA plasma instrument and in-flight calibration. *Space Science Reviews*, *141*(1–4), 277–302. https://doi.org/10.1007/s11214-008-9433-1

Meurant, M., Gérard, J.-C., Blockx, C., Spanswick, E., Donovan, E. F., Hubert, B., et al. (2007). EL—A possible indicator to monitor the magnetic field stretching at global scale during substorm expansive phase: Statistical study. *Journal of Geophysical Research*, *112*, A05222. https://doi.org/10.1029/2006JA012126

Morley, S., Koller, J., Welling, D., Larsen, B., & Niehof, J. (2014). SpacePy: Python-based tools for the space science community, Astrophysics Source Code Library.

Morley, S. K., Welling, D. T., Koller, J., Larsen, B. A., Henderson, M. G., & Niehof, J. (2011). SpacePy—A Python-based library of tools for the space sciences. In *Proceedings of the 9th Python in Science Conference* (pp. 39–45). Austin, TX. https://conference.scipy.org/proceedings/scipy2010/pdfs/morley.pdf

Newell, P. T., Sergeev, V. A., Bikkuzina, G. R., & Wing, S. (1998). Characterizing the state of the magnetosphere: Testing the ion precipitation maxima latitude (b2i) and the ion isotropy boundary. *Journal of Geophysical Research*, *103*, 4739–4745. https://doi.org/10.1029/97JA03622

Newell, P. T., Sotirelis, T., Liou, K., Meng, C.-I., & Rich, F. J. (2007). A nearly universal solar wind-magnetosphere coupling function inferred from 10 magnetospheric state variables. *Journal of Geophysical Research*, *112*, A01206. https://doi.org/10.1029/2006JA012015

Parzen, E. (1962). On estimation of a probability density function and mode. *Annals of Mathematical Statistics*, *33*(3), 1065–1076. https://doi.org/10.1214/aoms/1177704472

Peredo, M., Stern, D. P., & Tsyganenko, N. A. (1993). Are existing magnetospheric models excessively stretched? *Journal of Geophysical Research*, *98*(A9), 15343. https://doi.org/10.1029/93JA01150

Popova, T. A., Yahnin, A. G., Demekhov, A. G., & Chernyaeva, S. A. (2018). Generation of EMIC waves in the magnetosphere and precipitation of energetic protons: Comparison of the data from THEMIS high Earth orbiting satellites and POES low Earth orbiting satellites. *Geomagnetism and Aeronomy*, *58*(4), 469–482. https://doi.org/10.1134/S0016793218040114

Powell, K. G., Roe, P. L., Linde, T. J., Gombosi, T. I., & De Zeeuw, DarrenL (1999). A solution-adaptive upwind scheme for ideal magnetohydrodynamics. *Journal of Computational Physics*, *154*(2), 284–309. https://doi.org/10.1006/jcph.1999.6299

Ridley, A. J., Gombosi, T. I., & De Zeeuw, D. L. (2004). Ionospheric control of the magnetosphere: Conductance. *Annales Geophysicae*, *22*(2), 567–584.

Ridley, A. J., & Liemohn, M. W. (2002). A model-derived storm time asymmetric ring current driven electric field description. *Journal of Geophysical Research*, *107*(A8), 1151. https://doi.org/10.1029/2001JA000051

Sazykin, S. Y. (2000). Theoretical studies of penetration of magnetospheric electric fields to the ionosphere (Ph.D. Thesis), Utah State University, Logan, Utah.

Sergeev, V. A., Bikkuzina, G. R., & Newell, P. T. (1997). Dayside isotropic precipitation of energetic protons. *Annales Geophysicae*, *15*(10), 1233–1245.

Sergeev, V. A., Chernyaev, I. A., Angelopoulos, V., & Ganushkina, N. Y. (2015). Magnetospheric conditions near the equatorial footpoints of proton isotropy boundaries. *Annales Geophysicae*, *33*(12), 1485–1493. https://doi.org/10.5194/angeo-33-1485-2015

Sergeev, V. A., Chernyaeva, S. A., Apatenkov, S. V., Ganushkina, N. Y., & Dubyagin, S. V. (2015). Energy-latitude dispersion patterns near the isotropy boundaries of energetic protons. *Annales Geophysicae*, *33*(8), 1059–1070. https://doi.org/10.5194/angeo-33-1059-2015

Sergeev, V. A., & Gvozdevsky, B. B. (1995). MT-index–A possible new index to characterize the magnetic configuration of magnetotail. *Annales Geophysicae*, *13*(10), 1093–1103. https://doi.org/10.1007/s00585-995-1093-9

Sergeev, V. A., Kornilova, T. A., Kornilov, I. A., Angelopoulos, V., Kubyshkina, M. V., Fillingim, M., et al. (2010). Auroral signatures of the plasma injection and dipolarization in the inner magnetosphere. *Journal of Geophysical Research*, *115*, A02202. https://doi.org/10.1029/2009JA014522

Sergeev, V. A., Malkov, M., & Mursula, K. (1993). Testing the isotropic boundary algorithm method to evaluate the magnetic field configuration in the tail. *Journal of Geophysical Research*, *98*(A5), 7609–7620. https://doi.org/10.1029/92JA02587

Sergeev, V. A., Sazhina, E. M., Tsyganenko, N. A., Lundblad, J. Å., & Søraas, F. (1983). Pitch-angle scattering of energetic protons in the magnetotail current sheet as the dominant source of their isotropic precipitation into the nightside ionosphere. *Planetary and Space Science*, *31*(10), 1147–1155. https://doi.org/10.1016/0032-0633(83)90103-4

Sergeev, V. A., & Tsyganenko, N. A. (1982). Energetic particle losses and trapping boundaries as deduced from calculations with a realistic magnetic field model. *Planetary and Space Science*, *30*(10), 999–1006.

Singer, H., Matheson, L., Grubb, R., Newman, A., & Bouwer, D. (1996). Monitoring space weather with the GOES magnetometers. In E. R. Washwell (Ed.), *Proceedings of SPIE* (Vol. 2812, pp. 299–308). Denver, CO: International Society for Optics and Photonics. https://doi.org/10.1117/12.254077

Søraas, F. (1972). ESRO IA/B observations at high latitudes of trapped and precipitating protons with energies above 100 keV, *Earth's magnetospheric processes* (pp. 120–132). Dordrecht: Springer. https://doi.org/10.1007/978-94-010-2896-712

Søraas, F., Aarsnes, K., Oksavik, K., & Evans, D. S. (2002). Ring current intensity estimated from low-altitude proton observations. *Journal of Geophysical Research*, *107*(A7), 1149. https://doi.org/10.1029/2001JA000123

Søraas, F., Lundblad, J. Å., Maltseva, N. F., Troitskaya, V., & Selivanov, V. (1980). A comparison between simultaneous I.P.D.P. groundbased observations and observations of energetic protons obtained by satellites. *Planetary and Space Science*, *28*(4), 387–405. https://doi.org/10.1016/0032-0633(80)90043-4

Tapping, K. F. (2013). The 10.7 cm solar radio flux (F 10.7). *Space Weather*, *11*, 394–406. https://doi.org/10.1002/swe.20064

Toffoletto, F., Sazykin, S., Spiro, R., & Wolf, R. (2003). Inner magnetospheric modeling with the Rice Convection Model. *Space Science Reviews*, *107*(1–2), 175–196.

Tóth, G., Sokolov, I. V., Gombosi, T. I., Chesney, D. R., Clauer, CRobert, De Zeeuw, D. L, et al. (2005). Space Weather Modeling Framework: A new tool for the space science community. *Journal of Geophysical Research*, *110*, A12226. https://doi.org/10.1029/2005JA011126

Tsyganenko, N. A. (1982). Pitch-angle scattering of energetic particles in the current sheet of the magnetospheric tail and stationary distribution functions. *Planetary and Space Science*, *30*(5), 433–437. https://doi.org/10.1016/0032-0633(82)90052-6

Tsyganenko, N. A. (1989). A magnetospheric magnetic field model with a warped tail current sheet. *Planetary and Space Science*, *37*(1), 5–20. https://doi.org/10.1016/0032-0633(89)90066-4

Tsyganenko, N. A. (2002). A model of the near magnetosphere with a dawn-dusk asymmetry 1. Mathematical structure. *Journal of Geophysical Research*, *107*(A8), 1179. https://doi.org/10.1029/2001JA000219

Tsyganenko, N. A., & Andreeva, V. A. (2016). An empirical RBF model of the magnetosphere parameterized by interplanetary and ground-based drivers. *Journal of Geophysical Research: Space Physics*, *121*, 10,786–10,802. https://doi.org/10.1002/2016JA023217

Tsyganenko, N. A., & Sitnov, M. I. (2005). Modeling the dynamics of the inner magnetosphere during strong geomagnetic storms. *Journal of Geophysical Research*, *110*, A03208. https://doi.org/10.1029/2004JA010798

Welling, D. T., & Liemohn, M. W. (2016). The ionospheric source of magnetospheric plasma is not a black box input for global models. *Journal of Geophysical Research: Space Physics*, *121*, 5559–5565. https://doi.org/10.1002/2016JA022646

West, H. I., Buck, R. M., & Kivelson, M. G. (1978). On the configuration of the magnetotail near midnight during quiet and weakly disturbed periods: Magnetic field modeling. *Journal of Geophysical Research*, *83*(A8), 3819. https://doi.org/10.1029/JA083iA08p03819

Wolf, R. A., Harel, M., Spiro, R. W., Voigt, G.-H., Reiff, P. H., & Chen, C. K. (1982). Computer simulation of inner magnetospheric dynamics for the magnetic storm of July 29, 1977. *Journal of Geophysical Research*, *87*(A8), 5949–5962.

Yahnin, A. G., & Yahnina, T. A. (2007). Energetic proton precipitation related to ion-cyclotron waves. *Journal of Atmospheric and Solar-Terrestrial Physics*, *69*(14), 1690–1706. https://doi.org/10.1016/j.jastp.2007.02.010

Yue, C., Wang, C.-P., Lyons, L., Liang, J., Donovan, E. F., Zaharia, S. G., & Henderson, M. (2014). Current sheet scattering and ion isotropic boundary under 3-D empirical force-balanced magnetic field. *Journal of Geophysical Research: Space Physics*, *119*, 8202–8211. https://doi.org/10.1002/2014JA020172

Zhang, Y., Paxton, L. J., & Zheng, Y. (2008). Interplanetary shock induced ring current auroras. *Journal of Geophysical Research*, *113*, A01212. https://doi.org/10.1029/2007JA012554